Available online at www.sciencedirect.com
SCIENCE DIRECT®
International Journal of Heat and Mass Transfer 47 (2004) 3245–3256
International Journal of HEAT and MASS TRANSFER
www.elsevier.com/locate/ijhmt

Magnetohydrodynamic free convection and entropy generation in a square porous cavity

Shohel Mahmud *, Roydon Andrew Fraser

Department of Mechanical Engineering, University of Waterloo, 200 University Avenue West, Waterloo, Ont., Canada N2L3G1

Received 19 September 2003; received in revised form 6 February 2004
Available online 20 March 2004

Abstract

The problem of entropy generation in a fluid saturated porous cavity for laminar magnetohydrodynamic natural convection heat transfer is analyzed in this paper. Heat transfer results are also presented additionally. Darcy's law for porous media is considered. Magnetic force is assumed acting along the direction of the gravity force. As boundary conditions of the cavity, two vertical opposite walls are kept at constant but different temperatures and the remaining two walls are kept thermally insulated. For a range of Rayleigh number ($Ra = 1$–10^4) and Hartmann number ($Ha = 0$–10), heat transfer, overall entropy generation rate, and heat transfer irreversibility are presented in terms of dimensionless Nusselt number (Nu), entropy generation number (Ns), and Bejan number (Be), respectively. Finally, parametric results are presented in terms of isothermal lines, streamlines, isentropic lines, and iso-Bejan lines.

1. Introduction

Natural convection heat transfer inside a square and/or rectangular cavity is not a new problem for research. A rich and variety of experimental, numerical, and analytical results have been published for last two/three decades due to its importance in many engineering applications, including heating and cooling of rooms, nuclear and electronic equipment cooling, etc. The research of natural convection in porous media has been conducted widely in recent years, which involves post-accidental heat removal in nuclear reactors, cooling of radioactive waste containers, heat exchangers, solar power collectors, grain storage, food processing, energy efficient drying processes, to name of a few. The process of manufacturing materials in industrial problems and microelectronic heat transfer devices involve an electrically conducting fluid subjected to a magnetic field. In that case the fluid experiences a Lorentz force and its effect is to reduce the flow velocities. This in turn affects the rate of heat and mass transfer. It is, therefore, important to study the detailed characteristics of transport phenomena in such a process so that good quality product can be developed with improved design in the manufacturing processes. For a good and comprehensive reference of above mentioned topics, see articles by Yang [1], Kulacki et al. [2], and Bejan [3].

Most of the published articles related to the cavity problem are restricted, in the thermodynamic point of view, to only First-law (of thermodynamics) analysis. The contemporary trend in the field of heat transfer and thermal design is Second-law (of thermodynamics) analysis and its design-related concept of entropy generation and its minimization [4]. Entropy generation minimization (EGM) is the method of modeling and optimization of real devices that owe their thermodynamic imperfection to heat transfer, mass transfer, and fluid flow irreversibilities. It is also known as "thermodynamic optimization" in engineering, where it was first developed, or more recently as "finite time thermodynamics" in the physics literature. The method combines from the start the most basic principles of thermodynamics, heat transfer, and fluid mechanics.

* Corresponding author. Tel.: +1-519-886-9589; fax: +1-519-888-6197.
E-mail addresses: smahmud@uwaterloo.ca (S. Mahmud), rafraser@uwaterloo.ca (R.A. Fraser).

0017-9310/$ - see front matter © 2004 Elsevier Ltd. All rights reserved.
doi:10.1016/j.ijheatmasstransfer.2004.02.005

Nomenclature

A	aspect ratio of the cavity
A_c	cross-sectional area of the cavity (m^2)
B_0	downward component of the magnetic force ($Wb\,m^{-2}$)
Be	Bejan number, Eq. (10)
C_p	specific heat at constant pressure ($J\,kg^{-1}\,K^{-1}$)
C_s	specific heat of the solid ($J\,kg^{-1}\,K^{-1}$)
Ec	Eckert number, $= u_0^2 C_p/\Delta T$
g	gravitational acceleration ($m\,s^{-2}$)
FFI	fluid friction irreversibility
h	convective heat transfer coefficient ($W\,m^{-2}\,K^{-1}$)
Ha	Hartmann number, $= B_0\sqrt{\sigma_e K/\mu}$
HTI	heat transfer irreversibility
k	thermal conductivity of the fluid ($W\,m^{-1}\,K^{-1}$)
K	permeability of the porous media (m^2)
L	length and width of the cavity (m)
Ns	entropy generation number, $= S'''_{gen}/S'''_0$
Nu	Nusselt number, $= hL/k$
Pr	Prandtl number, $= \mu C_p/k$
Ra	Darcy-modified Rayleigh number, Eq. (3)
Ra^*	Darcy–Hartmann-modified Rayleigh number, $= Ra/(1+Ha^2)$
S'''_0	characteristic transfer rate, $= k(\Delta T)^2/(LT_0)^2$ ($W\,m^{-3}\,K^{-1}$)
S'''_{gen}	local entropy generation rate ($W\,m^{-3}\,K^{-1}$)
t	time (s)
T	temperature of the fluid (°C)
u	velocity component at x-direction ($m\,s^{-1}$)
U	dimensionless velocity component at x-direction
v	velocity component at y-direction ($m\,s^{-1}$)
V	dimensionless velocity component at y-direction
u_0	reference velocity, $= \alpha L$
x	distance along the x-coordinate (m)
X	distance along the dimensionless x-coordinate
y	distance along the y-coordinate (m)
Y	distance along the dimensionless y-coordinate

Greek symbols

α	thermal diffusivity of the fluid ($m^2\,s^{-1}$)
β	volumetric coefficient of thermal expansion (K^{-1})
δ	boundary layer thickness (m)
μ	dynamic viscosity of the fluid (Pa s)
ν	kinematic viscosity of the fluid ($m^2\,s^{-1}$)
ρ	density of the fluid ($kg\,m^{-3}$)
ρ_s	density of the solid ($kg\,m^{-3}$)
ϕ	porosity of the porous media
ψ	streamfunction ($m^2\,s^{-1}$)
Ψ	dimensionless streamfunction, $= \psi/\alpha$
σ	an empirical constant, Eq. (3)
σ_e	fluid electrical conductivity ($\Omega^{-1}\,m^{-1}$)
Θ	dimensionless temperature, Eq. (3)
τ	dimensionless time, Eq. (3)
Ω	dimensionless temperature difference, $= \Delta T/T_0$
$\forall$	volume of the cavity (m^3)

Subscripts and superscripts

av	average value
C	value at the cold wall
H	value at the hot wall
0	reference value

This new trend of optimization is important and, at the same time, necessary, if the heat transfer community is to contribute to a viable engineering solution to the energy problems. Entropy generation is associated with thermodynamic irreversibility, which is present in all types of heat transfer processes. Different sources of irreversibility are responsible for heat transfer's generation of entropy like heat transfer across finite temperature gradient, characteristics of convective heat transfer, viscous effects, etc. Bejan [4] focused on the different reasons behind entropy generation in applied thermal engineering. The generation of entropy destroys the available work of a system. Therefore, it makes good engineering sense to focus on the irreversibility of heat transfer and fluid flow processes, and try to understand the function of the entropy generation mechanism(s). Bejan [5] first presented the Second law aspect of heat transfer using different examples of fundamental forced convection problems. He introduced the concept of entropy generation number, irreversibility distribution ratio, and presented the spatial distribution of irreversibility, entropy generation profiles or maps for the example problems. Since then, numerous investigations have been carried out to determine the entropy generation and irreversibility profiles for different geometric configurations, flow situations, and thermal boundary conditions. Yilbas et al. [6] presented qualitative and quantitative results of entropy generation inside a differentially heated non-porous square cavity. For a porous cavity, Baytas [7] presented results of entropy generation at different orientations of a square cavity considering the Darcy model. Salas et al. [8] analytically showed a way of applying the entropy generation analysis for the modeling and optimization of MHD

induction devices. Salas et al. [8] restricted their analysis to only Hartmann model of flow in a channel. For a mixed convective flow, Mahmud et al. [9] gave a detailed analysis of the entropy generation nature and source of irreversibility in a vertical non-porous channel with transverse hydromagnetic effect. An extension of the above problem for porous media is available in Tasnim et al. [10]. For other geometric configurations and/or flow situations, an extensive review on Second-law analysis of fundamental problems of heat transfer are available in Mahmud and Fraser [11].

In the view of the above arguments, this study is conducted to examine the flow, temperature, and entropy generation fields inside a square porous cavity when subjected to natural convection due to differentially heated sidewalls and an applied magnetic field acted towards the direction of the gravity. The governing flow and energy equations are considered for two-dimensional laminar case. A numerical method is conducted based on control volume approach. The resulting Nusselt, entropy generation, and Bejan numbers' variation are investigated as a function of two independent parameters: Rayleigh number and Hartmann number.

2. Problem formulation

Consider the flow of a Newtonian fluid within a square porous enclosure as shown in Fig. 1. The non-dimensional governing equations are obtained with following assumptions: (a) the cavity is completely filled with porous material, (b) Darcy's law is assumed to hold, (c) the fluid is assumed to be a normal Boussinesq-incompressible fluid, (d) negligible inertial effects, (e) the saturated porous medium is assumed to be isotropic in thermal conductivity, and (f) magnetic force is acting along the direction of the gravity. Finally, the set of non-dimensional governing equations in terms of the stream function (Ψ) and temperature (Θ) are as follows

$$\frac{\partial^2 \Psi}{\partial X^2} + (1 + Ha^2)\frac{\partial^2 \Psi}{\partial Y^2} = -Ra\frac{\partial \Theta}{\partial X}, \tag{1}$$

$$\frac{\partial \Theta}{\partial \tau} + \frac{\partial \Psi}{\partial Y}\frac{\partial \Theta}{\partial X} - \frac{\partial \Psi}{\partial X}\frac{\partial \Theta}{\partial Y} = \frac{\partial^2 \Theta}{\partial X^2} + \frac{\partial^2 \Theta}{\partial Y^2}, \tag{2}$$

where the dimensionless variables are defined by

$$(X, Y) = \left(\frac{x}{L}, \frac{y}{L}\right), \quad (U, V) = \left(\frac{u}{\alpha/L}, \frac{v}{\alpha/L}\right), \quad \Psi = \frac{\psi}{\alpha},$$
$$\tau = \left(\frac{\alpha}{\sigma L^2}\right)t, \quad Ra = \frac{g\beta\Delta T L K}{\alpha v}, \quad \Theta = \frac{T - T_C}{T_H - T_C},$$
$$Ha = B_0\sqrt{\frac{\sigma_e K}{\mu}}, \quad \sigma = \frac{\phi\rho C_p + (1-\phi)\rho_s C_s}{\rho C_p}. \tag{3}$$

The non-dimensional streamfunction, Ψ, satisfies the following equations

$$\frac{\partial \Psi}{\partial Y} = U \quad \text{and} \quad \frac{\partial \Psi}{\partial X} = -V. \tag{4}$$

Eqs. (1) and (2) are subjected to the following boundary conditions:

$$\begin{aligned} &Y = 0 \text{ and } 0 \leqslant X \leqslant 1 : \Psi = 0 \text{ and } \partial\Theta/\partial Y = 0,\\ &Y = 1 \text{ and } 0 \leqslant X \leqslant 1 : \Psi = 0 \text{ and } \partial\Theta/\partial Y = 0,\\ &X = 0 \text{ and } 0 \leqslant Y \leqslant 1 : \Psi = 0 \text{ and } \Theta = 0,\\ &X = 1 \text{ and } 0 \leqslant X \leqslant 1 : \Psi = 0 \text{ and } \Theta = 1. \end{aligned} \tag{5}$$

Eqs. (1) and (2) along with the boundary conditions given in Eq. (5) are solved using a control volume based finite-volume method [12]. A non-staggered and non-uniform grid system is used with a higher mesh density near the walls. TDMA solver solves discretized and linearized equation systems. For unsteady terms, Crank–Nicolson method is applied. The whole computational domain is subdivided by an unequally spaced rectangular mesh. Four grid sizes (32×32, 64×64, 100×100, and 128×128) are chosen for analysis. Average Nusselt number for all four grid sizes are monitored at $Ra = 10^3$ and $Ha = 0$. The magnitude of average Nusselt number at 128×128 grids shows a very little difference with the result obtained at 100×100 grids. For rest of the calculation in this paper we chose a grid size of 128×128 for better accuracy. The time increment ($\Delta\tau$) was 10^{-4} in most cases; but sometimes, especially at high Ra smaller values were chosen in order to confirm the accuracy of the results.

For the benchmarking purpose, a differentially heated square porous cavity with zero magnetic forces is

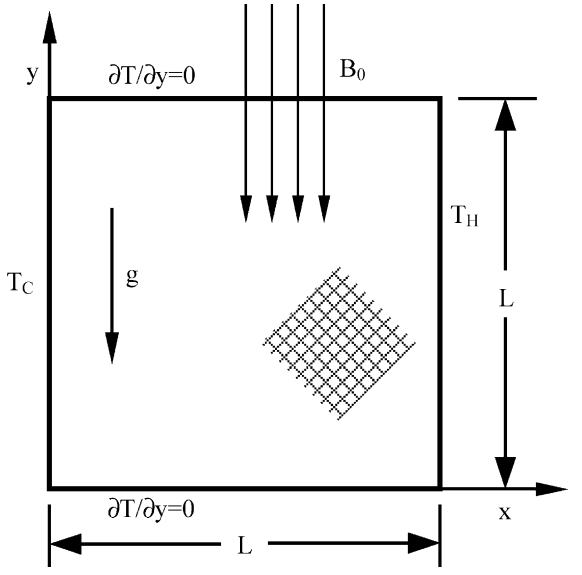

Fig. 1. Schematic diagram of the problem under consideration.

Table 1
Comparison of average Nusselt number with some previous numerical results

	Nu_{av}		
	$Ra = 10$	$Ra = 100$	$Ra = 1000$
Baytas and Pop [13]	1.079	3.16	14.06
Walker and Homsy [14]	–	3.10	12.96
Gross et al. [15]	–	3.14	13.45
Manole and Lage [16]	–	3.12	13.64
Moya et al. [17]	1.065	2.80	–
Present prediction	1.079	3.14	13.82

considered. Average Nusselt number is calculated for three different Rayleigh numbers ($Ra = 10$, 100, and 1000) and compared with the available published works by Baytas and Pop [13], Walker and Homsy [14], Gross et al. [15], Manole and Lage [16], and Moya et al. [17]. This comparison is shown in Table 1. It is seen from Table 1 that the agreement between the present and the previous results is very good. Therefore, we are confidant that the numerical method used and the results presented in this paper are very accurate.

3. Entropy generation

The dimensionless form of entropy generation rate (S'''_{gen}) is termed as entropy generation number [4]. Entropy generation number (Ns) is the ratio between the volumetric entropy generation rate (S'''_{gen}) and a characteristics transfer rate (S'''_0). The characteristics transfer rate for the present problem can be estimated from the following equation:

$$S'_0 = \frac{k(\Delta T)^2}{L^2 T_0^2}. \tag{6}$$

For the porous media, which follows the Darcy model, the local rate of entropy generation (S'''_{gen}) can be calculated from the following equation:

$$S'''_{gen} = \frac{k}{T_0^2}(\nabla T)^2 + \frac{\mu}{KT_0}(\mathbf{V})^2 + \frac{1}{T_0}[(\mathbf{J} - Q\mathbf{V}) \cdot (\mathbf{E} + \mathbf{V} \times \mathbf{B})],$$

where

$$\mathbf{J} = \sigma_e(\mathbf{E} + \mathbf{V} \times \mathbf{B}). \tag{7}$$

The detailed derivation of the above equation is available in Woods [18]. In Eq. (7), $\mathbf{J}$, Q, $\mathbf{V}$, $\mathbf{E}$, $\mathbf{B}$, σ_e, and T_0 are electric current, electric charge density, velocity vector, electric field, magnetic induction, fluid's electrical conductivity, and reference temperature, respectively. It is assumed that in the effective current density term ($\mathbf{J} - Q\mathbf{V}$) of Eq. (7), $\mathbf{J} \gg Q\mathbf{V}$. Similarly, the electric force per unit charge ($\mathbf{E}$) is assumed negligible compared to the magnetic force per unit charge ($\mathbf{V} \times \mathbf{B}$). Eq. (7) can be simplified for the present problem in the following form:

$$S'_{gen} = \frac{k}{T_0^2}\left[\left(\frac{\partial T}{\partial x}\right)^2 + \left(\frac{\partial T}{\partial y}\right)^2\right] + \frac{\mu}{KT_0}(u^2 + v^2) + \frac{\sigma_e B_0^2}{T_0}u^2, \tag{8}$$

which can be expressed in its dimensionless form by the following expression:

$$Ns = \frac{S'''_{gen}}{S'''_0} = \left[\left(\frac{\partial \Theta}{\partial X}\right)^2 + \left(\frac{\partial \Theta}{\partial Y}\right)^2\right] + \frac{Ec \times \mathrm{Pr}}{\Omega}\left[\left(\frac{\partial \Psi}{\partial X}\right)^2 + \left(\frac{\partial \Psi}{\partial Y}\right)^2 + Ha^2\left(\frac{\partial \Psi}{\partial Y}\right)^2\right], \tag{9}$$

where Ec, Pr, and Ω are the Eckert number, Prandtl number, and dimensionless temperature difference, respectively. As a combination ($Ec \times Pr/\Omega$), these three parameters together are termed a group parameter. Eq. (9) consists of two parts. The first part (first square bracketed term at the right-hand side of Eq. (9)) is the irreversibility due to finite temperature gradient and generally termed as the heat transfer irreversibility (HTI). The second part (second square bracketed term) is the contribution of fluid friction irreversibility (FFI) to entropy generation. The overall entropy generation, for a particular problem, is an internal competition between HTI and FFI. Usually, free convection problems, at low and moderate Rayleigh numbers, are dominated by the heat transfer irreversibility. Entropy generation number (Ns) is good for generating entropy generation profiles or maps but fails to give any idea whether fluid friction or heat transfer dominates. Two alternate parameters, irreversibility distribution ratio (Φ) and Bejan number (Be), are achieving an increasing popularity among the Second-Law analysts. Bejan number (Be), which is the ratio of HTI to the total entropy generation (Ns), can be mathematically expressed as

$$Be = \frac{\mathrm{HTI}}{\mathrm{HTI} + \mathrm{FFI}}. \tag{10}$$

Bejan number ranges from 0 to 1. Accordingly, $Be = 1$ is the limit at which the heat transfer irreversibility dominates, $Be = 0$ is the opposite limit at which the irreversibility is dominated by fluid friction effects, and

$Be = 1/2$ is the case in which the heat transfer and fluid friction entropy generation rates are equal.

4. Results and discussion

The parameters which influence the flow, heat transfer, and entropy generation rate inside the cavity are Rayleigh number, Hartmann number, group parameter, and Prandtl number. Both Rayleigh and Hartmann numbers are preferred as independent variables, while the Prandtl number is kept constant throughout this investigation. However, the group parameter ($Ec \times Pr/\Omega$) depends on the fluid and flow properties and hence there is an indirect relation with Rayleigh and Hartmann numbers. Group parameter is automatically adjusted by the numerical code once a change is done on Rayleigh and Hartmann numbers.

5. Flow and thermal field

For the special case, $Ha = 0$, flow and thermal fields' results are available in Baytas [7] for a square cavity and Baytas and Pop [13] for square and oblique cavities. With a few exceptional cases these results will not be repeated here.

Streamlines inside the cavity is shown in Fig. 2(a)–(c) for three different values of Hartmann numbers, $Ha = 0$, 5, and 10, for $Ra = 100$. Corresponding isothermal lines are presented in Fig. 2(d)–(f). For $Ra = 100$, convection current inside the cavity is well set. A counterclockwise circulation appears (Fig. 2(a)) due to the effect of upward moving fluid near the hot wall and downward moving fluid near the cold wall. In the absence of any magnetic force ($Ha = 0$), the usual convective distortion of the isothermal lines occurs (Fig. 2(d)) with two thermal spots: one at the bottom of the hot wall and another at the top of the cold wall. Magnitude of the heat flux is higher at theses two spots due to higher temperature gradient. The distortion of isothermal lines appears due the high convective current inside the cavity. An introduction of a magnetic force acting along the direction of the gravity force tends to retard the fluid motion inside the cavity. For a constant Rayleigh number, strength of circulation (presented by ψ_{max}) inside the cavity reduces with increasing Hartmann number. As Hartmann number increases, a large portion of the fluid in the middle portion of the cavity becomes almost motionless. This is supported by the elongated–stagnant core of the

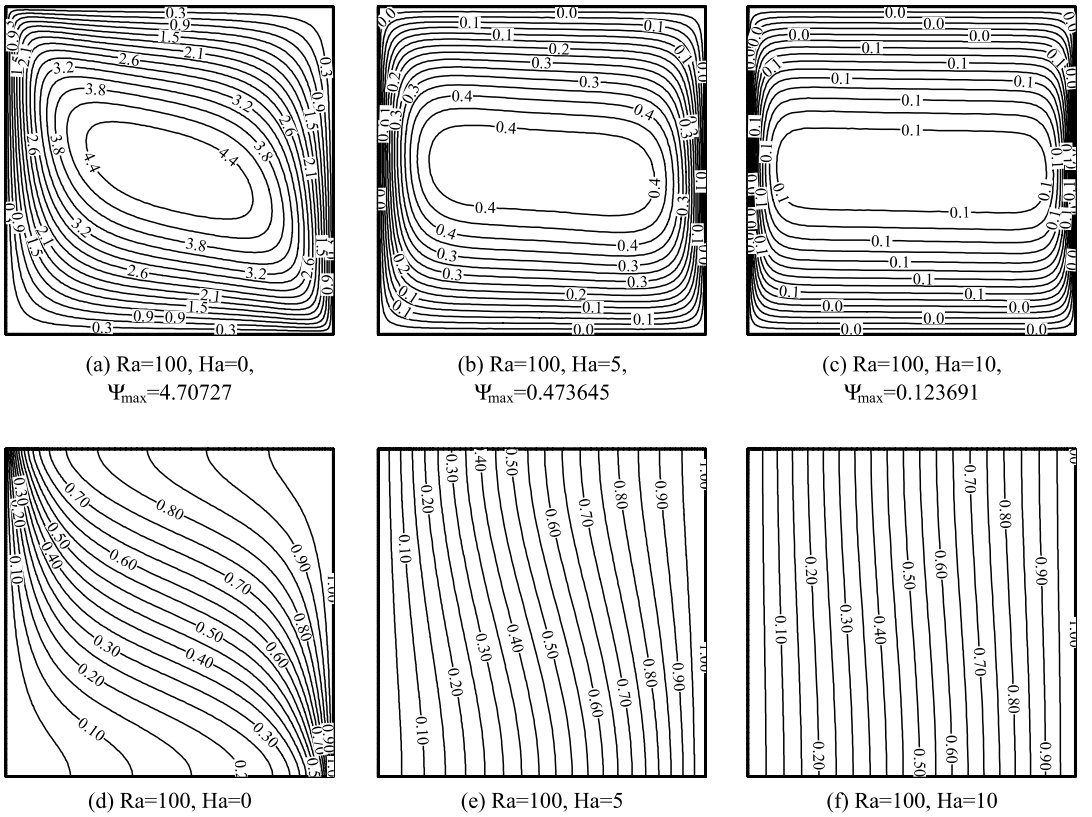

(a) Ra=100, Ha=0, Ψ_{max}=4.70727 (b) Ra=100, Ha=5, Ψ_{max}=0.473645 (c) Ra=100, Ha=10, Ψ_{max}=0.123691

(d) Ra=100, Ha=0 (e) Ra=100, Ha=5 (f) Ra=100, Ha=10

Fig. 2. Streamlines and isothermal lines at $Ra = 100$.

streamline with increasing Hartmann number at $Ra = 100$. Distortion of isothermal lines as well as thermal spots also start to disappear with increasing Hartmann number. As Hartmann number increases, isothermal lines inside the cavity approaches more and more towards the conduction-like distribution pattern (Fig. 2(e) and (f)) of isothermal lines. For large Hartmann number ($Ha = 10$), Fig. 2(f) indicates that the convection is almost suppressed, and the isotherms are almost parallel to the vertical wall, indicating that a quasiconduction regime is reached.

An explanation of the above behavior can be possible by a scale analysis [19], which is purely mathematical in nature. However, a physical explanation will be given later. To perform a scale analysis, the non-dimensional form of the momentum equation (Eq. (1)) is converted into its dimensional form using different definitions given in Eqs. (3) and (4). This dimensional form can be written as

$$\left(1+\frac{B_0^2\sigma_e K}{\mu}\right)\frac{\partial u}{\partial y}-\frac{\partial v}{\partial x}=-\frac{Kg\beta}{\nu}\frac{\partial T}{\partial x}. \tag{11}$$

Assuming the following scales for changes in x, y, and T : $x \sim \delta$, $y \sim L$, and $T \sim \Delta T$ are valid. Using the scaling factors, the momentum equation together with the continuity equation can be written in the following forms:

momentum:

$$\left(1+\frac{B_0^2\sigma_e K}{\mu}\right)\frac{u}{L},\frac{v}{\delta}\sim\frac{Kg\beta}{\nu}\frac{\Delta T}{L}, \tag{12a}$$

continuity:

$$\frac{u}{\delta}\sim\frac{v}{L}. \tag{12b}$$

The two inertia terms at the left-hand side of Eq. (12a) are balanced by the buoyancy term at the right-hand side. The main objective of the scale analysis is to find a simple but logical relationship between the velocity components (u and v) and two dominating independent parameters: Rayleigh number (Ra) and Hartmann number (Ha). A close observation of Eq. (12a) reveals that the terms associated with the magnetic force appear with the velocity component u. A balance between the first inertia term and the buoyancy term (of Eq. (12a)) constitutes a scale of velocity component u in the following form

$$u\sim\frac{Kg\beta L}{\nu(1+B_0^2\sigma_e K/\mu)}\frac{\Delta T}{\delta}=\left(\frac{\alpha}{\delta}\right)\frac{Ra}{1+Ha^2}=\left(\frac{\alpha}{\delta}\right)Ra^*, \tag{13}$$

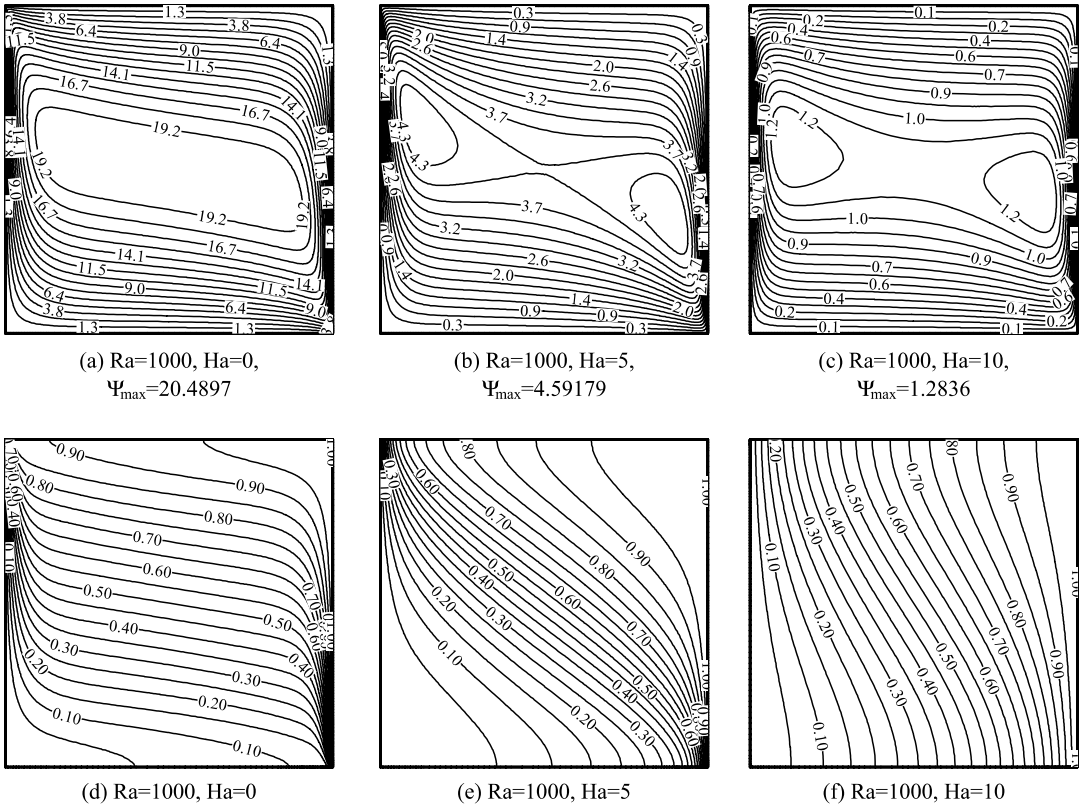

(a) Ra=1000, Ha=0, Ψ_{max}=20.4897

(b) Ra=1000, Ha=5, Ψ_{max}=4.59179

(c) Ra=1000, Ha=10, Ψ_{max}=1.2836

(d) Ra=1000, Ha=0

(e) Ra=1000, Ha=5

(f) Ra=1000, Ha=10

Fig. 3. Streamlines and isothermal lines at $Ra = 1000$.

and with the aid of Eqs. (12b) and (13) the scale factor for velocity component v is

$$v \sim \left(\frac{L\alpha}{\delta^2}\right)\frac{Ra}{1+Ha^2} = \left(\frac{L\alpha}{\delta^2}\right)Ra^*. \tag{14}$$

Eqs. (13) and (14) have two different Rayleigh numbers: Ra and Ra^*. Bejan [19] defines the first Rayleigh number (Ra) as Darcy-modified Rayleigh number due the presence of the permeability (K) term in its definition (see Eq. (3)). Ra^* is proposed to be the Darcy–Hartmann-modified Rayleigh number and which is the ratio between Ra and $(1+Ha^2)$. The proportionality between the velocity components (u and v) and Ra^* concludes that an increasing Hartmann number reduces the magnitudes of the velocity components inside the cavity as long as the Darcy-modified Rayleigh number is kept constant. In reality, a downward acting magnetic force suppresses the buoyancy force and its action is similar to a drag force; hence reducing the magnitudes of the velocity components. The scale of the dimensionless streamfunction (Ψ) is given by the following:

$$\Psi \sim \frac{v\delta}{\alpha} \sim \left(\frac{L}{\delta}\right)\frac{Ra}{1+Ha^2} = \left(\frac{L}{\delta}\right)Ra^*, \tag{15}$$

which is proportional to the flow rate (see Poulikakos and Bejan [20]). For a constant Darcy-modified Rayleigh number, Ψ decreases with increasing Hartmann number, i.e., a reduction of the circulation strength inside the cavity. This argument is also supported by the decreasing magnitude of $\Psi_{\max}$ (as reported at the bottom of Figs. 2 and 3) with increasing Hartmann number. Fig. 3(a)–(c) shows the streamline distribution for $Ra = 1000$ at $Ha = 0$, 5, and 10. Corresponding isothermal lines are shown in Fig. 3(d)–(f). At $Ha = 0$, the flow field comprises a unicellular flow of relatively high velocity, circulating around the entire cavity. A large and extended portion of the fluid at the middle section of the cavity is motionless, which is a characteristics flow feature at $Ra = 1000$ as obtained by other researchers, for example Baytas [7]. Because of boundary layer effects, sharp drops in temperature near the vertical walls (Fig. 3(d)) characterize the temperature field. Thermal spots are elongated (compared to Fig. 2(d)) near hot and cold walls at this Rayleigh number. If the magnetic field is relatively strengthened, the flow circulation is progressively inhibited by the retarding effect of the magnetic body force. Two egg shaped cores appear at $Ha = 5$. Convective distortion of isothermal lines starts to disappear with increasing Hartmann number as before. Length of thermal spots are shortened at $Ha = 5$ and disappeared at $Ha = 10$. At $Ha = 10$, size of the core increases with decreasing center to center vertical distance between two cores.

6. Heat transfer

Heat transfer's result is presented in terms of the global Nusselt number (Nu_{av}) which is obtained by

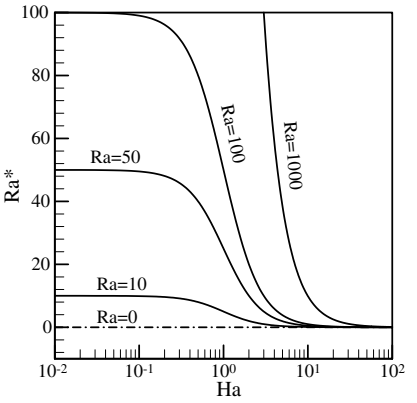

Fig. 4. Ra^* as a function of Ha at different Ra.

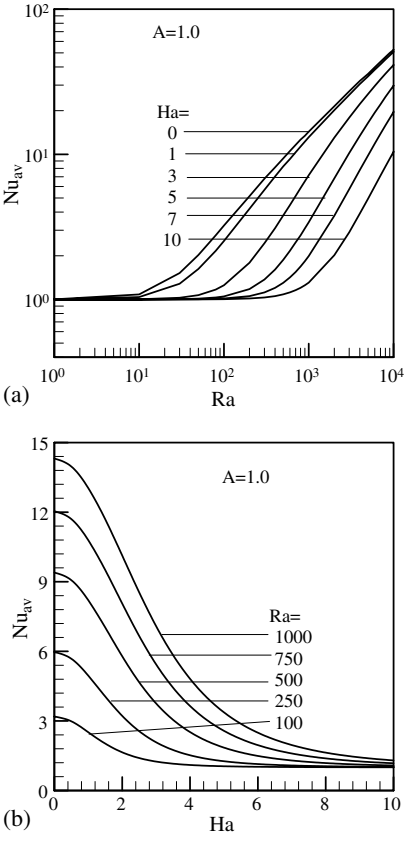

Fig. 5. (a) Average Nusselt number as a function of Rayleigh number. (b) Average Nusselt number as a function of Hartmann number.

integrating the local Nusselt number (Nu_L) as shown in the following equation:

$$Nu_{av} = \int_0^1 Nu_L \, dY,$$

where

$$Nu_L = \left(\frac{k}{\Delta T}\right)\left.\frac{\partial T}{\partial x}\right|_{x=0} = \left.\frac{\partial \Theta}{\partial X}\right|_{X=0}, \quad (16)$$

where k is the thermal conductivity of the fluid. To visualize the variation of heat transfer inside the cavity a range of Rayleigh number ($Ra = 10^0$–10^4) and Hartmann number ($Ha = 0$–10) is selected. The justification of using the selected range of Hartmann number will be discussed first before presenting the heat transfer's result. It was already shown that the parameters (for example u, v, Ψ, etc.) considered in this investigation have a direct relation with Darcy–Hartmann-modified Rayleigh number (Ra^*), which is a ratio between Ra and $(1 + Ha^2)$. For two limiting cases of Hartmann number, $Ha \to 0$ and $Ha \to \infty$, Ra^* approaches to Ra and 0, respectively. The lower limit ($Ha \to 0$) is considered in our investigation. However, to set a finite value for the upper limit of the Hartmann number, the behavior of the Ra^* is monitored with the variation of Ha at different Ra. Fig. 4 shows this monitored result. Three distinct locations are identified in the Ra^*–Ha profiles depending on the value of Hartmann number. For $Ha < 0.3$, Ra^*'s distribution is almost independent of Ha and its value is almost equal to Ra. For the range of Hartmann number, $0.3 \leqslant Ha \leqslant 10$, Ra^* decreases rapidly with increasing Ha. An asymptotic behavior is observed in the Ra^*–Ha profiles for $Ha > 10$. One can notice that the variation of Ra^* with Ha is insignificant beyond $Ha = 10$ for all Ra. So, using $Ha = 10$ as the upper limit for the range of Hartmann number is justified.

Average Nusselt number is plotted as a function of Rayleigh number in Fig. 5(a) at different values of Hartmann number. Two distinct zones are identified in the Nu_{av}–Ra profiles depending on the value of Rayleigh number. In the conduction-dominated zone, distribution of Nu_{av} is independent of the Rayleigh number's increment and the magnitude of Nu_{av} is equal to 1. In the convection-dominated zone, Nu_{av} increases almost linearly in logarithmic plot with increasing Rayleigh number. The extent of the conduction-dominated zone increases with increasing Hartmann number. In the convection-dominated zone, higher Hartmann number shows a lower value of average heat transfer. A scaling argument may be applied to visualize heat transfer's

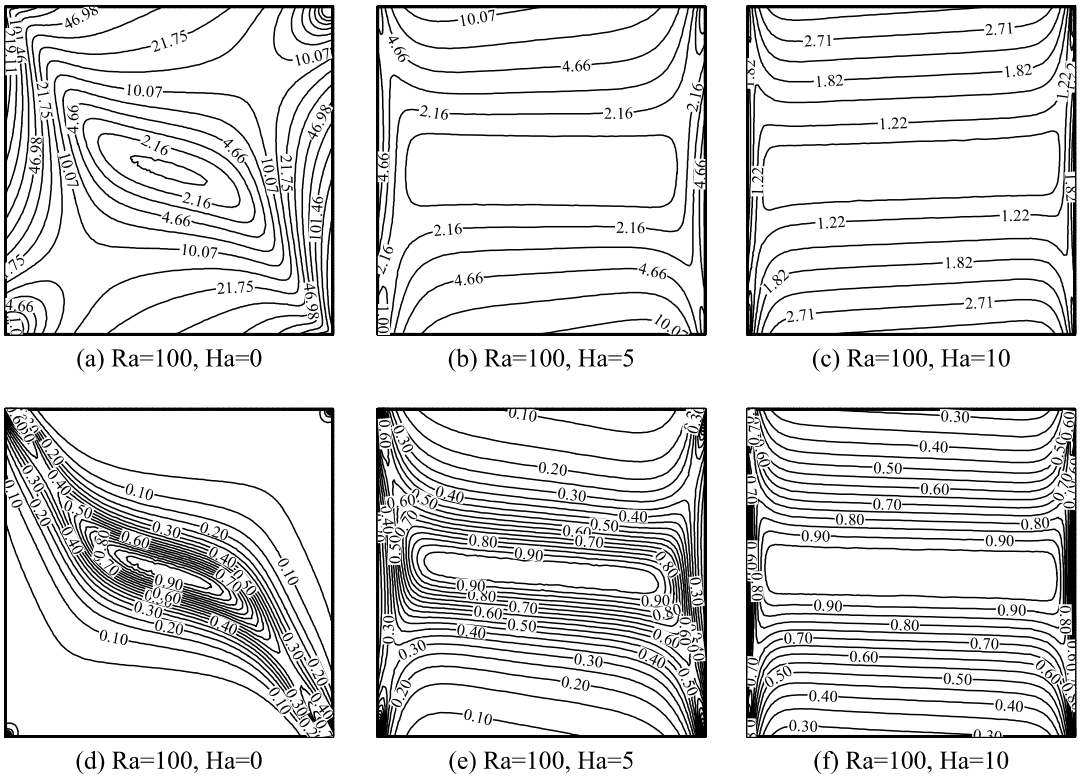

(a) Ra=100, Ha=0 (b) Ra=100, Ha=5 (c) Ra=100, Ha=10

(d) Ra=100, Ha=0 (e) Ra=100, Ha=5 (f) Ra=100, Ha=10

Fig. 6. Isentropic lines and iso-Bejan lines at $Ra = 100$.

variation with Ra, Ha, or Ra^*. According to Bejan [19], the volumetric flowrate driven horizontally, in counter-flow is of order $v\delta$; this stream carries enthalpy between the two vertical walls at a rate

$$Q_{\text{convection}} \sim \rho C_p v\delta\Delta T \sim \rho C_p \Delta T\left(\frac{L\alpha}{\delta}\right)\frac{Ra}{1+Ha^2}. \qquad (17)$$

From the above expression, one can easily identify the decreasing tendency of heat transfer rate with increasing Ha as long as Ra is constant. The variation of Nu_{av} as a function of Hartmann number for five different Rayleigh numbers is shown in Fig. 5(b). Heat transfer rate is maximum at $Ha = 0$. Once a magnetic force is introduced and strengthened, average Nusselt number (Nu_{av}) decreases rapidly and approaches its asymptotic value ($=1$). For smaller Ra, Nu_{av} approaches $Nu_{\text{av}} = 1$ for smaller value of Ha as shown in Fig. 5(b).

7. Entropy generation

The dimensionless forms of local entropy generation rate (Ns) and heat transfer irreversibility (Be) are calculated using Eqs. (9) and (10) once the values of Ψ and Θ are available from the converged solution. Contours of Ns (isentropic lines) and Be (iso-Bejan lines) for $Ra = 100$ and $Ha = 0$, 5, and 10 are presented in Fig. 6(a)–(f), respectively.

At $Ha = 0$ (Fig. 6(a)), entropy generation spreads all over the cavity. Entropy generation rate is lower in magnitude around the center of the cavity. Entropy generates at a higher magnitude near the cavity walls. Both of the vertical walls act as strong concentrators of irreversibility due to higher values of near wall velocity components and temperature gradient. In the presence of magnetic force, the magnitude of entropy generation rate is reduced. Vertical walls no longer act as strong concentrators of irreversibility. A significant portion of the cavity, extended along the horizontal direction at the mid-height of the cavity, acts as an *idle region for entropy generation* (see Mahmud and Fraser [21] and Das et al. [22]) where entropy generation rate is zero or negligible (see Fig. 6(b) and (c)). In the absence of the magnetic force, a region along the diagonal that connecting the top corner of the cold wall and the bottom corner of the hot wall shows high heat transfer irreversibility (Fig. 6(d)). It should be noted that a large portion of the fluid at this region is either stagnant or slower in motion leaving a negligible contribution of fluid friction irreversibility (FFI) on overall entropy

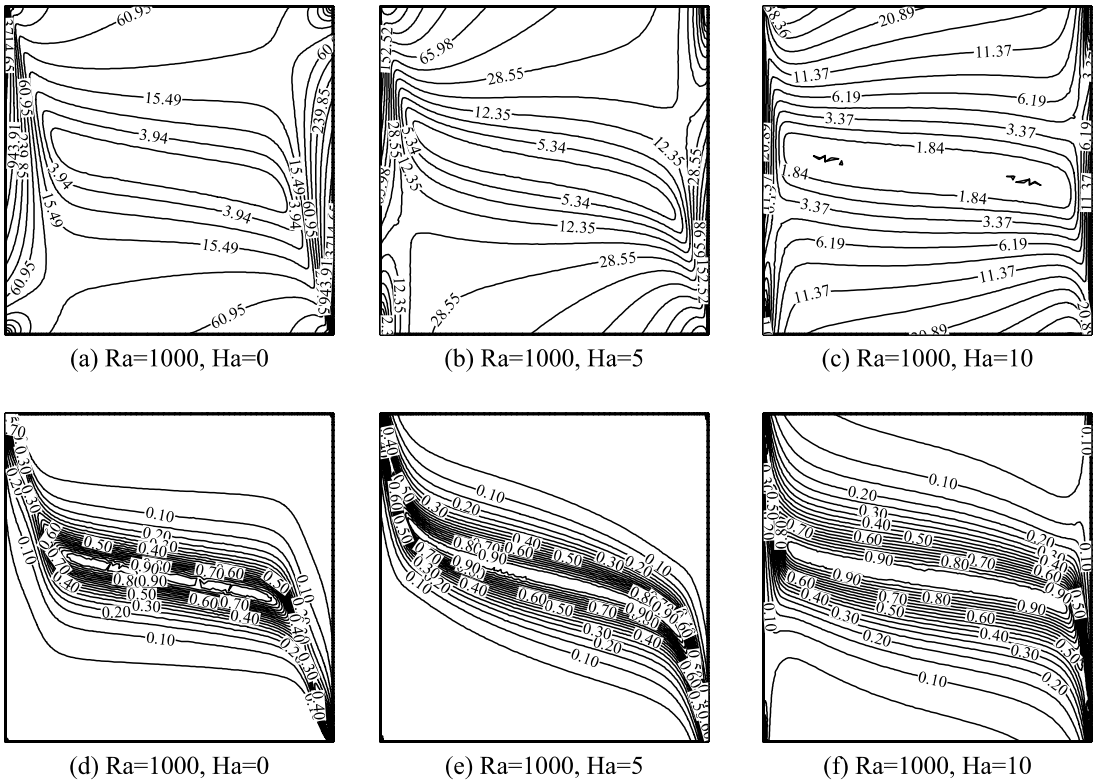

Fig. 7. Isentropic lines and iso-Bejan lines at $Ra = 1000$.

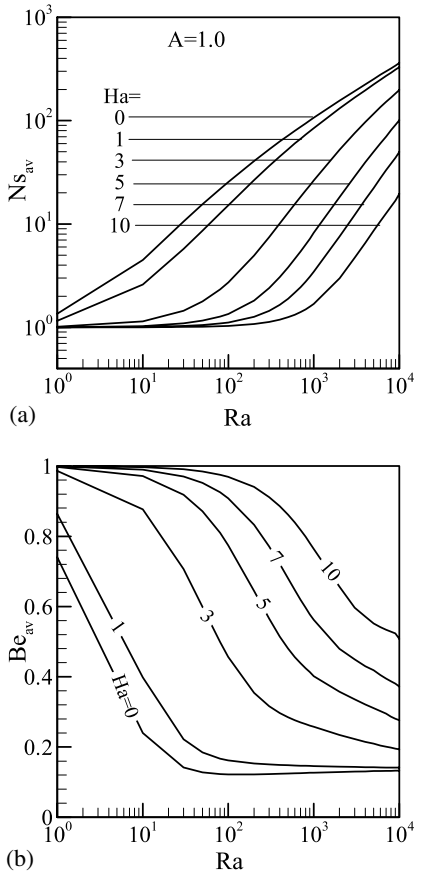

Fig. 8. (a) Average entropy generation number as a function of Rayleigh number. (b) Average Bejan number as a function of Rayleigh number.

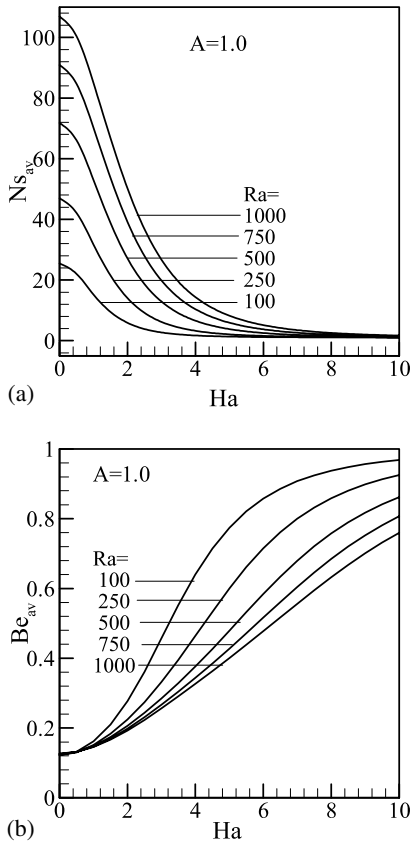

Fig. 9. (a) Average entropy generation number as a function of Hartmann number. (b) Average Bejan number as a function of Hartmann number.

generation rate (*Ns*). Thus, Bejan number, a ratio between the heat transfer irreversibility and overall entropy generation, shows higher values along this diagonal region. Heat transfer irreversibility spreads all over the domain after introducing the magnetic force. The similarity between the distribution pattern of contours of *Ns* and *Be* at $Ha = 5$ and 10 indicates a dominance of the heat transfer irreversibility over the fluid friction irreversibility.

The above results for $Ra = 1000$ are presented in Fig. 7(a)–(c) isentropic lines and Fig. 7(d)–(f) for iso-Bejan lines. In the absence of a magnetic field (see Fig. 7(a)), only a very thin region near two vertical walls acts as a strong concentrator of irreversibility with a relatively higher magnitude of *Ns*. Almost same pattern of entropy generation is observed at $Ha = 5$, but the magnitude of *Ns* is low. Similar distribution pattern is observed at $Ha = 10$. Bejan number at $Ha = 0$ (Fig. 7(d)) shows the same diagonal dominance as is observed in Fig. 6(d). The region occupied by Bejan contours thickens as the magnetic force is introduced and strengthened. The local entropy generation number (*Ns*) would be integrated over the whole domain to obtained the volume averaged (or global) entropy generation rate inside the cavity as shown in the following equation

$$Ns_{\mathrm{av}} = \frac{1}{\forall}\int_{\forall} Ns\,\mathrm{d}\forall = \frac{1}{A_{\mathrm{c}}}\int_0^1\int_0^1 Ns(X,Y)\,\mathrm{d}X\,\mathrm{d}Y, \qquad (18)$$

where $\forall$ and A_{c} are the volume and the cross-sectional area of the cavity, respectively. Similarly, average Bejan number can be obtained from the following equation:

$$Be_{\mathrm{av}} = \frac{1}{\forall}\int_{\forall} Be\,\mathrm{d}\forall = \frac{1}{A_{\mathrm{c}}}\int_0^1\int_0^1 Be(X,Y)\,\mathrm{d}X\,\mathrm{d}Y. \qquad (19)$$

Fig. 8(a) and (b) show the distribution of Ns_{av} and Be_{av} as a function of Rayleigh number at different Hartmann numbers as indicated in the figure. For $Ha = 0$ and 1, average entropy generation rate increases with increasing Rayleigh number. However, the behavior of the Ns_{av}–*Ra* profiles is similar to the Nu_{av}–*Ra* profiles for $Ha > 1$. Two zones are identified in the Ns_{av}–*Ra* profiles: a region with invariable Ns_{av} (region 1) and then a region

with linearly varying (in logarithmic plot) Ns_{av} (region 2). At low and moderate Rayleigh numbers with magnetic force, conduction dominates. Most of the contribution on overall entropy generation comes from the heat transfer irreversibility. Average Bejan number shows a value closer to 1 (see Fig. 8(b)). Thus, the variation of Ns_{av} with increasing Ra is insignificant in region 1. A significant contribution on entropy generation comes from the fluid friction irreversibility at comparatively higher Ra (region 2) due to high convection current. A simultaneous increase of Ns_{av} and decrease of Be_{av} characterize the nature of irreversibility at high Ra. Higher Hartmann number shows lower entropy generation rate and higher heat transfer irreversibility at a particular Rayleigh number in region 2. Fig. 9(a) and (b) show the variation of Ns_{av} and Be_{av} as a function of Ha at different Ra. Similar to the Nu_{av}–Ha profile characteristics, Ns_{av} is maximum at $Ha = 0$, decreases with increasing Ha and approaches an asymptote at higher values of Hartmann number. Magnitudes of Be_{av} are almost same for all Rayleigh numbers considered here at $Ha = 0$. Increases in the value of Ha have a tendency to slowdown the fluid movement inside the cavity, thus causing a relative increases of heat transfer irreversibility (i.e., Be_{av}).

8. Conclusions

We investigated numerically the First and Second Laws (of thermodynamics) aspects of fluid flow and heat transfer inside a porous cavity subjected to a magnetic field acting along the direction of the gravity. A scale analysis is also presented to ease our understanding about flow and thermal fields' behavior and heat transfer rate inside the cavity. The effect of Rayleigh and Hartmann numbers is tested on average Nusselt number, entropy generation number, and Bejan number. Increases in the value of Ha (i.e. magnetic force) have a tendency to retard the fluid motion inside the cavity. Both Nu_{av} and Ns_{av} decrease with increasing Ha and approach a limiting value (asymptotic value). In the absence of magnetic force, entropy generation rate is relatively higher in magnitude near two vertical walls. Entropy generation rate is decreased in magnitude as the magnetic force is introduced and strengthened. Local Bejan number's distribution shows a diagonal dominance. Average Bejan number distribution with Ra or Ha shows an opposite behavior when compared with Ns_{av}.

References

[1] K.T. Yang, Natural convection in enclosures, in: S. Kakac, R.K. Shah, W. Aung (Eds.), Handbook of Single-Phase Convective Heat Transfer, Wiley, New York, 1987 (Chapter 13).

[2] F.A. Kulacki, J.H. Davidson, P.F. Dunn, Convective heat transfer with electric and magnetic field, in: S. Kakac, R.K. Shah, W. Aung (Eds.), Handbook of Single-Phase Convective Heat Transfer, Wiley, New York, 1987 (Chapter 9).

[3] A. Bejan, Convection heat transfer in porous media, in: S. Kakac, R.K. Shah, W. Aung (Eds.), Handbook of Single-Phase Convective Heat Transfer, Wiley, New York, 1987 (Chapter 16).

[4] A. Bejan, Entropy Generation Minimization, CRC Press, New York, 1996.

[5] A. Bejan, A study of entropy generation in fundamental convective heat transfer, J. Heat Transfer 101 (1979) 718–725.

[6] B.S. Yilbas, S.Z. Shuja, S.A. Gbadebo, H.I.A. Hamayel, K. Boran, Natural convection and entropy generation in a square cavity, Int. J. Energy Res. 22 (1998) 1275–1290.

[7] A.C. Baytas, Entropy generation for natural convection in an inclined porous cavity, Int. J. Heat Mass Transfer 43 (2000) 2089–2099.

[8] S. Salas, S. Cuevas, M.L. Haro, Entropy generation analysis of magnetohydrodynamic induction devices, J. Phys. D: Appl. Phys. 32 (1999) 2605–2608.

[9] S. Mahmud, S.H. Tasnim, M.A.H. Mamun, Thermodynamic analysis of mixed convection in a channel with transverse hydromagnetic effect, Int. J. Therm. Sci. 42 (2003) 731–740.

[10] S.H. Tasnim, S. Mahmud, M.A.H. Mamun, Entropy generation in a porous channel with hydromagnetic effect, Exergy 2 (2002) 300–308.

[11] S. Mahmud, R.A. Fraser, The second law analysis in fundamental convective heat transfer problems, Int. J. Therm. Sci. 42 (2003) 177–186.

[12] J.H. Ferziger, M. Perić, Computational Methods for Fluid Dynamics, Springer-Verlag, New York, 1996.

[13] A.C. Baytas, I. Pop, Free convection in oblique enclosures filled with a porous medium, Int. J. Heat Mass Transfer 42 (1999) 1047–1057.

[14] K.L. Walker, G.M. Homsy, Convection in a porous cavity, J. Fluid Mech. 87 (1978) 449–474.

[15] R.J. Gross, M.R. Bear, C.E. Hickox, The application of flux-corrected transport (FCT) to high Rayleigh number natural convection in porous medium, in: Proc. 8th International Heat Transfer Conference, San Francisco, CA, 1986.

[16] D.M. Manole, J.L. Lage, Numerical benchmark results for natural convection in a porous medium cavity, HTD-Vol. 216, Heat and Mass Transfer in Porous Media, ASME Conference, 1992, pp. 55–60.

[17] S.L. Moya, E. Ramos, M. Sen, Numerical study of natural convection in a tilted rectangular porous material, Int. J. Heat Mass Transfer 30 (1987) 741–756.

[18] L.C. Woods, The Thermodynamics of Fluid Systems, Oxford University Press, Oxford, 1975.

[19] A. Bejan, Convection Heat Transfer, Wiley, New York, 1984.

[20] D. Poulikakos, A. Bejan, Penetrative convection in porous medium bounded by a horizontal wall with hot

and cold spots, Int. J. Heat Mass Transfer 27 (1984) 1749–1757.

[21] S. Mahmud, R.A. Fraser, Second law analysis of heat transfer and fluid flow inside a cylindrical annular space, Exergy 2 (2002) 322–329.

[22] P.K. Das, S. Mahmud, S.H. Tasnim, A.K.M.S. Islam, Effect of surface waviness and aspect ratio on heat transfer inside a wavy enclosure, Int. J. Numer. Meth. Heat Fluid Flow 13 (2003) 1097–1122.